# Comparison of Structural, Thermodynamic, Kinetic and Mass Transport Properties of Mg$^{2+}$ Ion Models Commonly used in Biomolecular Simulations

Maria T. Panteva, George M. Giambaşu, and Darrin M. York*

The prevalence of Mg$^{2+}$ ions in biology and their essential role in nucleic acid structure and function has motivated the development of various Mg$^{2+}$ ion models for use in molecular simulations. Currently, the most widely used models in biomolecular simulations represent a nonbonded metal ion as an ion-centered point charge surrounded by a nonelectrostatic pairwise potential that takes into account dispersion interactions and exchange effects that give rise to the ion's excluded volume. One strategy toward developing improved models for biomolecular simulations is to first identify a Mg$^{2+}$ model that is consistent with the simulation force fields that closely reproduces a range of properties in aqueous solution, and then, in a second step, balance the ion–water and ion–solute interactions by tuning parameters in a pairwise fashion where necessary. The present work addresses the first step in which we compare 17 different nonbonded single-site Mg$^{2+}$ ion models with respect to their ability to simultaneously reproduce structural, thermodynamic, kinetic and mass transport properties in aqueous solution. None of the models based on a 12-6 nonelectrostatic nonbonded potential was able to reproduce the experimental radial distribution function, solvation free energy, exchange barrier and diffusion constant. The models based on a 12-6-4 potential offered improvement, and one model in particular, in conjunction with the SPC/E water model, performed exceptionally well for all properties. The results reported here establish useful benchmark calculations for Mg$^{2+}$ ion models that provide insight into the origin of the behavior in aqueous solution, and may aid in the development of next-generation models that target specific binding sites in biomolecules. © 2015 Wiley Periodicals, Inc.

DOI: 10.1002/jcc.23881

## Introduction

Magnesium ions are particularly important for nucleic acid systems in stabilizing tertiary structure,[1–3] driving folding processes,[4–7] and in the case of many ribozymes, playing a direct role in catalysis.[8–12] Due to the biological importance of divalent metal ions, much work has been done, especially in the last decade, to model these ions in molecular simulations.[13–16] As with many computational models, in order to be practical, rigor and complexity must be balanced with computational cost. For simulations of biological systems, care must be taken that the metal ion model keep pace, be balanced and easily integrated with the force field and water model that is being used to represent the rest of the system.

Currently, the most mature and commonly used biomolecular simulation force fields[17–26] are of the static charge, nonpolarizable form, and thus not able to explicitly account for multipolar electrostatics or quantum many-body effects.[27–33] Within this class of force fields, there have been two general strategies for constructing metal ion models based on bonded and nonbonded frameworks. Bonded metal ion models use empirical bonding terms to enforce the correct coordination structure, and cannot exchange their ligand environment.[34–36] Nonbonded metal ion models,[37] on the other hand, can exchange (at least in principle) in simulations,[38] and thus are more general in their potential application to processes where changes in coordination state or binding mode occur. Electrostatic interactions can be modeled in the traditional way with the ionic charge located at the nuclear center, or using multiple sites displaced from the nuclear center. The multisite models offer greater flexibility in distributing charges on the off-center sites, and have demonstrated considerable promise for improving coordination geometries, and selectivity of ion binding.[39–43] Nonetheless, currently the nonbonded models that are most widely used in biomolecular simulations represent a metal ion as an ion-centered point charge surrounded by a nonelectrostatic pairwise potential that takes into account dispersion interactions and most significantly, exchange effects that give rise to the ion's excluded volume. The most common form for the nonelectrostatic nonbonded pairwise potential is the Lennard–Jones potential[44] that has repulsive and attractive terms that vary as $r^{-12}$ and $r^{-6}$, respectively, where $r$ is the internuclear separation. Recently, several ion models have augmented this "12-6" potential with an additional $r^{-4}$ term, giving rise to a "12-6-4" potential that provides some

M. T. Panteva, G. M. Giambaşu, D. M. York
Center for Integrative Proteomics Research, BioMaPS Institute and Department of Chemistry & Chemical Biology, Rutgers University, 174 Frelinghuysen Road, Piscataway, New Jersey, 08854-8076
E-mail: york@biomaps.rutgers.edu

improvement.[16] Finally, another potentially useful approach for accounting for electronic polarization in nonpolarizable models is to scale partial charges by the inverse of the square root of the dielectric constant of the medium.[45–47] Although no such models exist to date for magnesium ions, parameters for calcium [48] and monovalents like lithium [49] and potassium [50] have been developed.

The ultimate goal of this work is to develop $Mg^{2+}$ ion models that provide a predictive understanding of the ion atmosphere around RNA that is integral to folding. The strategy that we take here is to first identify, or develop if necessary, a $Mg^{2+}$ model that is consistent with the RNA simulation force fields that closely reproduces a range of properties in aqueous solution. The second step, which is forthcoming, involves balancing the $Mg^{2+}$-water and $Mg^{2+}$-RNA interactions by tuning pairwise parameters for interactions at particular sites in RNA.[3]

In the present work, we explore the accuracy of a broad array of nonbonded single-site $Mg^{2+}$ ion models in molecular simulations. The main goal is to provide insight into the degree to which these ion models are able to simultaneously reproduce structural, thermodynamic, kinetic and mass transport properties in aqueous solution. To our knowledge, there has been no reported study to date that examines all of the $Mg^{2+}$ ion properties considered here, or that compares this wide range of $Mg^{2+}$ ion models together in one place with a consistent set of benchmark quality calculations (including error bars). None of the 17 models examined was able to exactly reproduce the experimental radial distribution function, solvation free energy, exchange barrier and diffusion constant, although the models based on a 12-6-4 potential (which have an additional parameter) offered improvement, and one model in particular, in conjunction with the SPC/E water model performed exceptionally well for all properties. The results reported here characterize the relative strengths and weaknesses of each model, and provide insight into the origin of their behavior that may aid in the development of next-generation models.

## Methods

All simulations have been carried out using the AMBER14 [17] simulation package and either the SPC/E,[51] TIP3P,[52] or TIP4-PEw [53] water models.

### Pairwise potential functional forms

In what follows, electrostatic interactions involving different ion models considered are simple Coulomb pair potentials, $\frac{q_i q_j}{r_{ij}}$, where $q_i$ and $q_j$ are charges located on particles $i$ and $j$, and $r_{ij}$ is the distance between the particles. As solvent is modeled explicitly, the dielectric constant in the Coulomb expression is unity. The only difference between the ion models is in the functional form of the nonelectrostatic pairwise potential and the parameters that adjust the interactions. These are described below.

The Lennard–Jones (12-6) potential [44] for nonbonded interactions is:

$$U_{ij}(r_{ij}) = \varepsilon_{ij} \left[ \left( \frac{R_{ij}}{r_{ij}} \right)^{12} - 2 \left( \frac{R_{ij}}{r_{ij}} \right)^{6} \right] \tag{1}$$

where the parameters $R_{ij}$ and $\varepsilon_{ij}$ are the combined radius and well depth for the pairwise interaction and $r_{ij}$ is the distance between the particles. Equation (1) can be expressed equivalently as:

$$U_{ij}(r_{ij}) = \frac{A_{ij}}{r_{ij}^{12}} - \frac{B_{ij}}{r_{ij}^{6}} \tag{2}$$

where $A_{ij} = \varepsilon_{ij} R_{ij}^{12}$ and $B_{ij} = 2\varepsilon_{ij} R_{ij}^{6}$.

The standard (12-6) potential can be augmented by an additional $r^{-4}$ term to form a (12-6-4) potential[16] as:

$$U_{ij}(r_{ij}) = \varepsilon_{ij} \left[ \left( \frac{R_{ij}}{r_{ij}} \right)^{12} - 2 \left( \frac{R_{ij}}{r_{ij}} \right)^{6} - 2\kappa R_{ij}^2 \left( \frac{R_{ij}}{r_{ij}} \right)^{4} \right]$$
$$= \frac{A_{ij}}{r_{ij}^{12}} - B_{ij} \left( \frac{1}{r_{ij}^{6}} + \frac{\kappa}{r_{ij}^{4}} \right) \tag{3}$$

where $\kappa$ is a scaling parameter with units of $\text{Å}^{-2}$. The difference between this potential and the 12-6 potential is the additional attractive term, $\kappa \frac{B_{ij}}{r_{ij}^{4}}$, which falls off as $r^{-4}$ and mimics the charge-induced dipole interaction.

### Existing $Mg^{2+}$ models

Table 1 summarizes the $Mg^{2+}$ ion models that will be considered in this study. The Lennard–Jones (LJ) parameters for these $Mg^{2+}$ models are characterized by a large radius (1.2–1.6 Å) and a very shallow well depth (0.0013–0.0266 kcal/mol), with the exception of the Åqvist model whose $r$ (0.7926 Å) and $\varepsilon$ (0.8947 kcal/mol) are comparatively small and large, respectively. The Åqvist model was originally parametrized with the SPC water model and the constrained spherical boundary model was used to treat the boundary as opposed to periodic boundary conditions.[54]

The Mayaan et al., Roux, Allnér et al., and Babu and Lim models were all parametrized using the modified TIP3P water model[57] (mTIP3P) which includes vdW radii on the hydrogens and is typically used in the CHARMM molecular dynamics package.[58] The Mayaan et al. model[55] aimed to get the correct structure and energetics of $Mg^{2+}$ binding to phosphates relative to water. The Roux model (results unpublished) is the $Mg^{2+}$ ion parameter set found in CHARMM and targets the absolute solvation free energy of $Mg^{2+}$, as referenced in the CHARMM parameter file for water and ions. Babu and Lim developed parameters by matching the experimental relative solvation free energy between $Cd^{2+}$ and $Mg^{2+}$.[14] The Allnér et al. model is the only parameter set which was parametrized against the experimental $Mg^{2+}$- water exchange rate.

More recently, a series of water model specific $Mg^{2+}$ parameters have been developed[15,16] and incorporated into AMBER for periodic boundary conditions using PME simulations. These new models include both 12-6 and 12-6-4 parameter sets. The 12-6-4 models target solvation free energy, $Mg^{2+}$-O

**Table 1.** Summary of the $Mg^{2+}$ models examined in this study. The parameters R, $\epsilon$ and $\kappa$ are described in the text. The main properties considered in the parametrization include: $R_{Mg^{2+}-O}$ (first solvation shell $Mg^{2+}$-O distance), RDF (radial distribution function), CN (coordination number), $\Delta G_{solv}$ (solvation free energy), $\Delta E$ (interaction energy) and $k_1$ (first shell water exchange rate).

| Model | R (Å) | $\epsilon$ (cal/mol) | $\kappa$ (Å$^{-2}$) | Water model | Properties[a] |
|---|---|---|---|---|---|
| Åqvist [54] | 0.7926 | 894.70000 | — | SPC | $\Delta G_{solv}$, RDF |
| Mayaan et al. [55] | 1.4647 | 14.00000 | — | mTIP3P[b] | structure, $\Delta E$[c] |
| Roux[d] | 1.1850 | 15.00000 | — | mTIP3P | $\Delta G_{solv}$ |
| Allnér et al. [56] | 1.5545 | 2.95000 | — | mTIP3P | $k_1$ |
| Babu and Lim [14] | 1.3636 | 26.60000 | — | mTIP3P | $\Delta G_{solv}$, $R_{Mg^{2+}-O}$, CN |
| Li et al. ($\Delta G_{solv}$ Set) [15] | 1.2080 | 1.26172 | — | TIP4PEw | |
| | 1.2840 | 3.95662 | — | TIP3P | $\Delta G_{solv}$ |
| | 1.2880 | 4.17787 | — | SPC/E | |
| Li et al. ($R_{Mg^{2+}-O}$ Set) [15] | 1.3950 | 14.91700 | — | TIP4PEw | |
| | 1.3950 | 14.91700 | — | TIP3P | $R_{Mg^{2+}-O}$ |
| | 1.3950 | 14.91700 | — | SPC/E | |
| Li et al. (CN Set) [15] | 1.3530 | 9.41798 | — | TIP4PEw | |
| | 1.3600 | 10.20237 | — | TIP3P | relative $\Delta G_{solv}$ and CN |
| | 1.3600 | 10.20237 | — | SPC/E | |
| Li and Merz 12-6-4 [16] | 1.4360 | 22.36885 | 1.362 | TIP4PEw | |
| | 1.4370 | 22.57962 | 1.046 | TIP3P | $\Delta G_{solv}$, $R_{Mg^{2+}-O}$, CN |
| | 1.4290 | 20.93385 | 0.987 | SPC/E | |

[a] Main properties considered in parametrization. [b] Includes vdW radii on hydrogens. [c] For $Mg^{2+}$ binding phosphates relative to water. [d] Unpublished results.

equilibrium distance and coordination number while their 12-6 counterparts typically only focus on one of these properties at a time.

## Calculation of Physical Properties

### Structure

Normalized radial distribution functions (RDFs), $g_{xy}(r)$,[59] give the probability of two particles (x and y) interacting at a specific distance (r) in solution relative to an ideal gas. Henceforth, we will focus on the distribution of water oxygens around the divalent ion, and designate the RDF simply as g(r). The peaks in the $Mg^{2+}$-O g(r) show the positions of the solvation shells around the ion, and the coordination numbers for the ith solvation shell are obtained by integrating g(r) as follows:

$$CN_i = 4\pi\rho \int_{r_{i-1}^{min}}^{r_i^{min}} g(r) r^2 dr; \quad r_0^{min} = 0 \quad (4)$$

where $\rho$ is the bulk particle density of the system and $r_1^{min}$, $r_2^{min}$ are the locations of the first and second minima in the RDFs, and $r_0^{min}$ is defined as zero.

### Thermodynamics

Desolvation free energies for $Mg^{2+}$ are computed using thermodynamic integration (TI) in two steps for the 12-6 models—first the charge is removed, then the vdW parameters. For the 12-6-4 models, an additional step to remove the charge-induced dipole contribution to the energy is included before removing charge.

For both the polarization and charge removing steps, the free energy difference between two states that have potential energies $V_0$ and $V_1$ and are linearly coupled is defined as [60]:

$$\Delta G_{TI} = \int_0^1 \langle \frac{dV(\lambda)}{d\lambda} \rangle_\lambda d\lambda; \quad V(\lambda) = \lambda V_0 + (1-\lambda)V_1 \quad (5)$$

where $\lambda$ is an order parameter that goes from 0 to 1, and 0 corresponds to the initial state and 1 corresponds to the end state. By running simulations at different $\lambda$ values one can obtain the quantity $\langle \frac{dV(\lambda)}{d\lambda} \rangle_\lambda$ directly and the integral in eq. (5) can be evaluated numerically.

In the final step, the $Mg^{2+}$ ion is decoupled from its environment completely and the form of the so called "softcore" potential is [61]:

$$V_{softcore} = 4\epsilon(1-\lambda) \left[ \frac{1}{\left[0.5\lambda + \left(\frac{r_{ij}}{\sigma}\right)^6\right]^2} - \frac{1}{0.5\lambda + \left(\frac{r_{ij}}{\sigma}\right)^6} \right] \quad (6)$$

where $r_{ij}$ is the distance between the disappearing $Mg^{2+}$ ion and the rest of the system and $\sigma$, which is equal to $\frac{R_{ij}}{2^{1/6}}$, is the contact distance at which the potential between the $Mg^{2+}$ ion and the other particles in the system vanishes.

### Kinetics

Transition state (TS) theory relates the rate constant (k) and the free energy of activation ($\Delta G^\dagger$) as:

$$k = Ae^{-\Delta G^\dagger/RT} \quad (7)$$

The pre-exponential factor, A, is in part a measure of the frequency of oscillation for a system about its minima and, for classical TS theory, is estimated to be equal to $k_BT/h$. Computationally, the prefactor can be estimated from the second derivative of the energy at the minimum ($E''$) of a potential of mean force (PMF) profile, $A = \frac{1}{2\pi}\sqrt{\frac{E''}{\mu}}$ where $\mu$ in the reduced mass of $Mg^{2+}$-O atom pair. The exponential term is a measure

of the probability that these oscillations have of crossing the barrier corresponding to an energy of $\Delta G^{\dagger}$.

We have applied transition state theory to estimate water exchange rates for the $Mg^{2+}$ ion models from free energy profiles generated with umbrella sampling simulations along the $Mg^{2+}$-O distance as a water exchange coordinate.

We employed the vFEP[62,63] method to calculate the free energy profiles from the simulation data and Jacobian corrections were applied. vFEP uses the maximum likelihood principle to determine a robust variational estimate for the free energy profile that is a global analytic function. vFEP does not require a high degree of overlap between umbrella windows and has been shown in many cases to have advantages over other methods such as MBAR[64] and WHAM.[65]

### Translational diffusion

The diffusion coefficient ($D$) is related to the mean squared displacement ($MSD$) through the Einstein relation[66]:

$$D = \lim_{\tau \to \infty} \frac{1}{6\tau} \langle |\mathbf{r}(t+\tau) - \mathbf{r}(t)|^2 \rangle \qquad (8)$$

where $t$ is the simulation time used in the average, $\tau$ is the time lag, $D$ is the diffusion coefficient and $\mathbf{r}$ is the position vector of the diffusing particle.

It has been previously shown that diffusion coefficients determined from simulations for water, metal ions, LJ liquids, and polymer chains are influenced by finite size effects under periodic boundary conditions.[67–71] A linear relationship between the inverse length of the simulation box and the computed diffusion coefficient can be used to extrapolate the diffusion coefficient ($D_o$) in the infinite dilution limit:

$$D_o = D_{PBC} + \frac{2.837297 k_B T}{6\pi\eta L} \qquad (9)$$

where $D_o$ represents the diffusion coefficient at infinite dilution. $D_{PBC}$ is the calculated diffusion coefficient for each box size, $k_B$ is Boltzmann's constant, $T$ is the temperature in K and $\eta$ is the solvent viscosity. $D_o$ can be calculated from the $y$-intercept of the $D_{PBC}$ versus $1/L$ plot, and the viscosity, $\eta$, can be determined from the corresponding slope. We will investigate the box size dependence of the diffusion coefficient for the SPC/E, TIP3P and TIP4PEw water models and all 17 $Mg^{2+}$ models using four box sizes.

## Simulation Protocols

All simulations were carried out using the AMBER14[17] molecular dynamics package. A 9 Å cutoff was applied to nonbonded interactions and the Particle Mesh Ewald (PME)[72] method was employed for the treatment of long range electrostatic interactions. Four box sizes were used in this study (541, 1029, 2311, 4395 total molecules), with box lengths of about 25, 31, 41, 51 Å, respectively. The equations of motion were integrated with a 1 fs time step and the target system temperature was set to 298 K. All covalent bonds involving hydrogen atoms were constrained with the SHAKE algorithm.[73]

Solvation free energies and exchange barriers were computed from NPT simulations while radial distribution functions and diffusion coefficients were obtained from NVT and NVT/NVE simulations, respectively. For the NPT simulations, the Berendsen barostat[74] was used to keep the pressure constant at 1 atm with a pressure relaxation time of 1 ps and the temperature was maintained by using the Langevin[75] thermostat with a collision frequency of 1 ps$^{-1}$. For the NVT simulations, the Berendsen thermostat was used instead with a coupling constant of 1 ps (unless otherwise noted in the text). For both NVT and NVE diffusion simulations, a more conservative SHAKE tolerance of $10^{-7}$ Å was enforced (compared to the default SHAKE tolerance in AMBER of $10^{-5}$ Å).

### *Ab initio* calculations

A high level quantum mechanical (QM) binding energy scan of the $Mg^{2+}$-oxygen distance of a $Mg^{2+}$ ion and one water molecule (with rigid TIP3P water geometry) was conducted at the counterpoise corrected MP2 level of theory along with the 6–31++G(d,p) basis set using the Gaussian 09 software package.[76] Rigid gas phase binding energy scans for all the $Mg^{2+}$ models, paired with their respective water model, were also performed in AMBER. For all scans, a 0.1 Å ion–oxygen separation distance interval was used.

### Radial distribution functions from simulation

$Mg^{2+}$-O radial distribution functions were calculated using data from 5.0 ns NVT simulations and with the $g(r)$ GUI plugin in VMD[77] with a bin spacing of 0.05 Å. RDFs were then further refined by fitting a cubic spline to the data points.

### Thermodynamic integration simulations

A total of three independent thermodynamic integration simulations[78] were performed for each set of $Mg^{2+}$ parameters and average desolvation free energies and standard deviations were obtained. $\lambda$ values ranged from 0 to 1 and were evenly spaced at 0.1 intervals for all steps. All $\lambda$ windows were equilibrated for 100 ps with the isothermal-isobaric ensemble, followed by 1 ns NPT production which was used for analysis.

### Umbrella sampling simulations

Umbrella sampling simulations for determination of water exchange barriers were started from a 1 ns NPT equilibrated system of $Mg^{2+}$ and water, where the reaction coordinate was chosen as the distance between the $Mg^{2+}$ ion and an inner sphere water oxygen. Stepwise equilibration for 20 ps was conducted for each umbrella window followed by 10 ns NPT production, of which the last 8 ns was ultimately used for analysis. Umbrella windows were positioned at 0.1 Å intervals from 1.8 to 6.0 Å. In addition, for the 12-6 potential models, whose PMF profiles were characterized by narrower peaks, windows were added around the transition state (0.05 Å intervals) to enhance sampling.

## Diffusion simulations

Ideally, diffusion coefficients should be computed from constant energy simulations which follow classical Newtownian dynamics. One technical drawback of NVE simulations, however, is that the average temperature of the simulation may not always be the desired target temperature (Supporting Information Fig. S3). Further, depending on the integration time step, integration algorithm and specific software implementation, NVE simulations may be prone to total energy drift over long time scales, which can affect values of dynamical properties.[79–81] A recent study[82] has shown that for NVT simulations velocity randomizing thermostats, such as Langevin[75] and Andersen,[83] significantly dampen the dynamics of the system when a small coupling constant is used while velocity rescaling thermostats such as Berendsen[74] and Nosé-Hoover[84–86] closely reproduce constant energy simulation results. It should also be noted that use of the Berendsen thermostat does not properly sample the Maxwell–Boltzmann distribution of kinetic energies.[87] Details on how different thermostats, thermostat coupling schemes and ensembles affect water and $Mg^{2+}$ diffusion results can be found in Supporting Information. The computed diffusion coefficients (Supporting Information Table S3) and temperature distributions (Supporting Information Fig. S2) for simulations in the NVE ensemble are very close to the NVT results, thus, we chose to run our diffusion simulations using the NVT ensemble.

All simulations were equilibrated for 1 ns in the NPT ensemble at which point the box size was fixed to the average volume obtained from the second half of the equilibration. Next, 5 ns of NVT equilibration was conducted followed by 21 ns of NVT production, the last 20 ns of which was used for analysis. The length of our diffusion simulations is 20 times longer than typical studies for $Mg^{2+}$ diffusion in the literature.[68,88]

Final box size dependent diffusion coefficients ($D_{PBC}$) were obtained in the following manner: (1) Each simulation is split into 20 1 ns segments (2) MSD$(\tau)$ vs $\tau$ plots are generated for each of the 20 1 ns segments where MSD$(\tau)$ is averaged over all molecules at 1 ps time lag intervals out to $\tau = 100$ ps 3) $D_{PBC}$ values are computed using the slope of the $<MSD>$ vs $\tau$ plot in the interval $20 \leq \tau \geq 80$ ps and subsequently averaged to yield the reported $D_{PBC}$ values and standard deviations. For the $Mg^{2+}$ models, 20 separate simulations of a single $Mg^{2+}$ ion in aqueous solution were performed for each box size and included in the calculation of $D_{PBC}$.

Diffusion coefficients at infinite dilution, and corresponding errors, were determined as the $y$-intercept of the size dependent data through linear regression by generating 1,000 data sets randomly extracted from the normal distribution of the box dependent values and obtaining the corresponding averages and standard deviations. The computed self-diffusion coefficients of $Mg^{2+}$ at infinite dilution ($D_o^{sim}$) were further scaled by a factor $\frac{D_o^w}{\tilde{D}_o^w}$, where $D_o^w$ and $\tilde{D}_o^w$ are the experimental and calculated water diffusion coefficients (Supporting Information Table S4), in order to correct for diffusion errors in the water models and make a more meaningful comparison with experiment.

## Results and Discussion

We present the results of a series of MD simulations comparing structural, thermodynamic, kinetic and mass transport properties of $Mg^{2+}$ ion models commonly used in biomolecular simulations. For each property, the $Mg^{2+}$ models are grouped by their respective water models (SPC/E, TIP3P, TIP4PEw), with the exception of the Åqvist model which was originally parametrized in SPC water but is included with the SPC/E $Mg^{2+}$ models in our study. It should also be noted that for all the ion models in the TIP3P water model group, the standard TIP3P water model available in AMBER is utilized for the calculations herein regardless of whether the ion model was originally parametrized with the mTIP3P water model (vdW radii on hydrogens) instead (Table 1). Supporting Information Tables S6–S9 suggest that there is a negligible water model-dependent effect between mTIP3P and TIP3P on the ion model properties studied here.

### Reference gas-phase $Mg^{2+}$-water binding energy scans

The gas phase energetics of a $Mg^{2+}$ ion with a single water molecule are of limited direct relevance to properties in aqueous solution. Nonetheless, analysis of the gas phase energy profiles yields simple properties such as zero energy (contact) distances, minimum energy distances and adiabatic binding energies that are correlated to certain bulk properties and help to facilitate later discussion. Rigid gas phase binding energy scans were obtained for $Mg^{2+}$-water dimers at 0.1 Å ion–oxygen separation distances in AMBER (Fig. 1).

In addition, a high level quantum mechanical (QM) binding energy scan (with rigid TIP3P water geometry) was conducted. Key features of the gas-phase $Mg^{2+}$-water interaction energy scans are listed in Table 2.

The quantum mechanical reference value for the minimum energy of a $Mg^{2+}$-water dimer ($-79.2$ kcal/mol) is generally more negative than the corresponding $Mg^{2+}$ model-water model values with one exception, the TIP4PEw Li et al. $\Delta G_{solv}$ model. At the same time, the minimum energy distance from the *ab initio* calculation (1.94 Å) is significantly larger than that obtained for the Li et al. $\Delta G_{solv}$ parameter set which has a similar minimum energy. These differences arise primarily from limitations in the static charge force fields which don't explicitly include polarization effects, and therefore do not respond sufficiently to the highly polarizing environment of a coordinated $Mg^{2+}$ ion.

Comparison of the Åqvist and Roux models, which are the default models in AMBER and CHARMM, respectively, indicates that the adiabatic binding energies at $-71.1$ and $-70.8$ kcal/mol and minimum energy distances at 1.89 and 1.85 Å are very similar. The strongest interaction energy within each water model category, however, belongs to the Li et al. $\Delta G_{solv}$ parameter sets which were parametrized against the experimental solvation free energy of $Mg^{2+}$. These three models also have the smallest $Mg^{2+}$-O minimum energy distances. Further, going from SPC/E and TIP3P to TIP4PEw, the gas phase binding energy becomes stronger by about 7 kcal/mol.
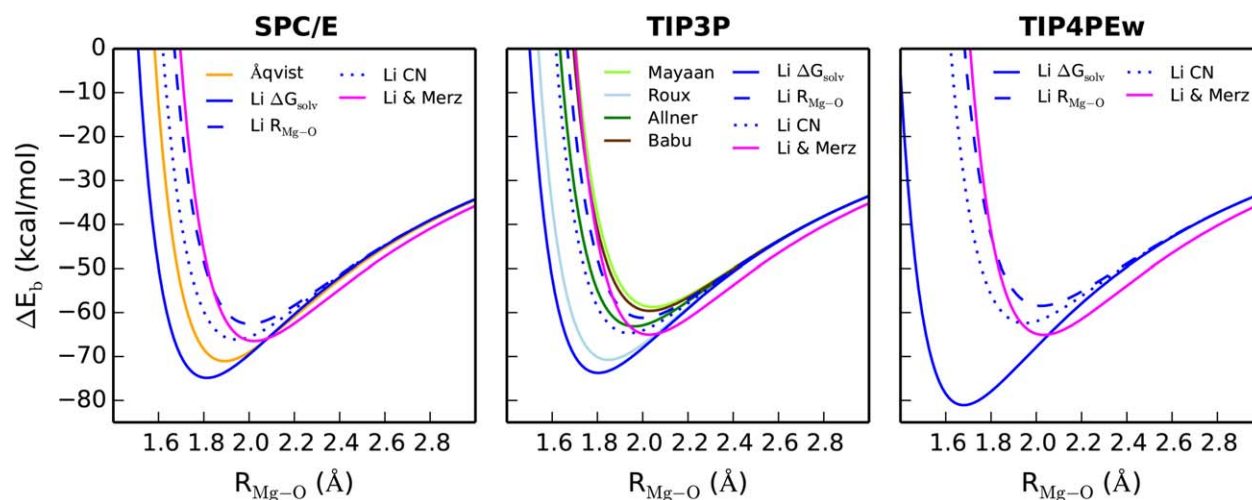
**Figure 1.** Total binding energy ($\Delta E_b$) of $Mg^{2+}$ with a single water molecule in the gas phase versus ion–oxygen separation distance ($R_{Mg^{2+}-O}$) for the $Mg^{2+}$ models and their respective water models.

When comparing the 12-6-4 models, we see that the minimum energy ranges between $-66.5$ kcal/mol (SPC/E) to about $-65$ kcal/mol (TIP3P/TIP4PEw), which for all water models, is less than the corresponding Li et al. $\Delta G_{solv}$ parameter sets. Contact distances ($\sigma$) are also correlated with minimum energy distances; the larger $R$, the larger $\sigma$.

A general correlation is observed between the binding energy in the gas phase and the solvation free energy of the 12-6 models (see Thermodynamics: Solvation free energy values section). A linear correlation also exists between the minimum energies distances from the adiabatic scans and the locations of the first solvation shell peaks in the RDFs (see Structure: $Mg^{2+}$-water oxygen radial distribution functions section).

### Structure: $Mg^{2+}$-water oxygen radial distribution functions

Various X-ray diffraction,[89–93] NMR,[94,95] and IR and Raman spectroscopic [96] studies have shown that $Mg^{2+}$ ions are hexacoordinated by water ligands in an octahedral geometry in aqueous solution. A first shell $Mg^{2+}$-O distance of $2.09 \pm 0.04$ Å, which is averaged over all available diffraction data collected in a comprehensive review by Marcus,[97] and a second shell range of 4.1–4.2 Å, also based on accumulated diffraction experiments in a review by Ohtaki and Radnai,[98] will be used as the reference values for all model comparisons.

The $Mg^{2+}$-O RDFs are illustrated for the 17 $Mg^{2+}$ models in Figure 2 and key properties are listed in Table 3. The RDFs illustrate the characteristically narrow first shell distribution and the wide, extended distribution of the second solvation shell. For all models, the second solvation shell peaks are very similar in shape and location. The main differences between the RDFs can be found in the first solvation shell, where the positions of the peaks are shifted relative to each other. For the TIP4PEw $Mg^{2+}$ models, the shapes of the first peak in the RDF vary as well. The maximum $g(r)$ in the first solvation shell is between 20–25 for all models except for the TIP4PEw

Li et al. $\Delta G_{solv}$ model, which has a maximum $g(r)$ closer to 15 (Table 3).

Table 3 summarizes the positions of the first and second solvation shell maxima and minima distances and the average coordination numbers for these shells. For the first solvation shell, peak distances range from 1.89 to 2.11 Å among the models while for the second solvation shell peak distances range from 4.09 to 4.37 Å. A general trend observed is that the closer the first solvation shell is to $Mg^{2+}$, the closer is the

**Table 2.** Key features of rigid $Mg^{2+}$-water interaction energy scans: "contact distance" ($\sigma$), minimum energy distance ($R$), and binding energy ($\epsilon$)

| $Mg^{2+}$ Model | Water Model | $\sigma$ (Å) | $R$ (Å) | $\epsilon$ (kcal/mol) |
|---|---|---|---|---|
| MP2/6–31++G(d,p)[a] | — | 1.45 | 1.94 | −79.2 |
| Åqvist | SPC/E | 1.58 | 1.89 | −71.1 |
| Li et al. $\Delta G_{solv}$ | SPC/E | 1.51 | 1.82 | −74.9 |
| Li et al. $R_{Mg^{2+}-O}$ | SPC/E | 1.67 | 2.01 | −62.6 |
| Li et al. CN | SPC/E | 1.62 | 1.94 | −66.1 |
| Li and Merz 12-6-4 | SPC/E | 1.70 | 2.02 | −66.5 |
| Mayaan et al. | TIP3P | 1.70 | 2.05 | −58.7 |
| Roux | TIP3P | 1.54 | 1.85 | −70.8 |
| Allnér et al. | TIP3P | 1.63 | 1.96 | −63.1 |
| Babu and Lim | TIP3P | 1.69 | 2.03 | −59.6 |
| Li et al. $\Delta G_{solv}$ | TIP3P | 1.50 | 1.80 | −73.7 |
| Li et al. $R_{Mg^{2+}-O}$ | TIP3P | 1.67 | 2.00 | −61.2 |
| Li et al. CN | TIP3P | 1.62 | 1.94 | −64.7 |
| Li and Merz 12-6-4 | TIP3P | 1.70 | 2.03 | −65.0 |
| Li et al. $\Delta G_{solv}$ | TIP4PEw | 1.39 | 1.68 | −81.1 |
| Li et al. $R_{Mg^{2+}-O}$ | TIP4PEw | 1.68 | 2.02 | −58.5 |
| Li et al. CN | TIP4PEw | 1.62 | 1.95 | −62.4 |
| Li and Merz 12-6-4 | TIP4PEw | 1.71 | 2.03 | −65.1 |

Note: Although an *ab initio* MP2 value is listed in the table for comparison, it is not meant to reflect a meaningful accuracy benchmark, and is not necessarily relevant to the solution properties that are the focus in this work. Nonetheless, as will be seen in later discussion, often the trends in different solution properties are simply related to trends of these simple indexes derived from the $Mg^{2+}$-water interaction curves, and therefore are useful to aid in the interpretation of the simulation results. [a] Reference QM binding energy scan was based on a rigid TIP3P water geometry and included counterpoise corrections.
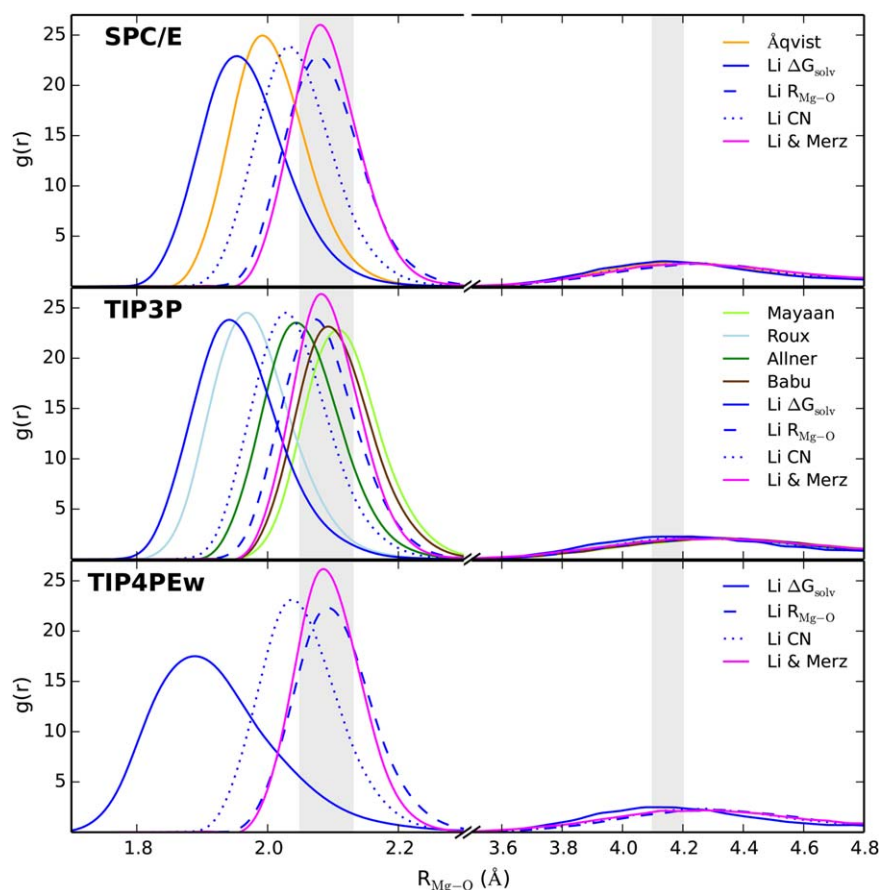
**Figure 2.** Normalized radial distribution functions for $Mg^{2+}$ models grouped by water model. Top: SPC/E, Middle: TIP3P, Bottom: TIP4PEw. Gray vertical lines at $2.09 \pm 0.04$ Å and 4.1–4.2 Å represent the ranges of experimental equilibrium $Mg^{2+}$-O distances for the first and second solvation shells, respectively.

second shell. The Li et al. $\Delta G_{solv}$ parameters have the tightest first solvation shells within their water model groups and do not fall within experimental error. In fact, the only models that

do match this property within experimental error are those which have been parametrized against it. That is, the Mayaan et al., Babu and Lim, and all the Li et al. $R_{Mg^{2+}-O}$ models from

**Table 3.** Summary of structural properties obtained from $Mg^{2+}$-water pair distribution functions. The first ($i = 1$) and second ($i = 2$) solvation shell peak maximum and minimum positions ($r_i^{max}$, $r_i^{min}$), their probabilities [$g(r_i^{max})$, $g(r_i^{min})$] and coordination numbers ($CN_i$) are compared, along with available experimental data. Distances are in units of Å.

| Model | Water Model | $r_1^{max}$ | $g(r_1^{max})$ | $r_1^{min}$ | $g(r_1^{min})$ | $CN_1$ | $r_2^{max}$ | $g(r_2^{max})$ | $r_2^{min}$ | $g(r_2^{min})$ | $CN_2$ |
|---|---|---|---|---|---|---|---|---|---|---|---|
| Åqvist | SPC/E | 1.99 | 24.9 | 2.49 | 0.0 | 6.0 | 4.18 | 2.5 | 4.93 | 0.7 | 13.6 |
| Li et al. $\Delta G_{solv}$ | SPC/E | 1.95 | 22.9 | 2.44 | 0.0 | 6.0 | 4.14 | 2.5 | 4.85 | 0.7 | 13.1 |
| Li et al. $R_{Mg^{2+}-O}$ | SPC/E | 2.08 | 22.9 | 2.59 | 0.0 | 6.0 | 4.26 | 2.3 | 4.96 | 0.7 | 13.7 |
| Li et al. CN | SPC/E | 2.03 | 23.8 | 2.39 | 0.0 | 6.0 | 4.24 | 2.3 | 4.9 | 0.7 | 13.3 |
| Li and Merz 12-6-4 | SPC/E | 2.08 | 26.0 | 2.48 | 0.0 | 6.0 | 4.22 | 2.3 | 4.99 | 0.8 | 14.3 |
| Mayaan et al. | TIP3P | 2.11 | 22.8 | 2.58 | 0.0 | 6.0 | 4.37 | 2.0 | 5.28 | 0.8 | 16.3 |
| Roux | TIP3P | 1.97 | 24.5 | 2.44 | 0.0 | 6.0 | 4.16 | 2.3 | 4.97 | 0.7 | 14.0 |
| Allnér et al. | TIP3P | 2.04 | 23.5 | 2.53 | 0.0 | 6.0 | 4.29 | 2.1 | 5.32 | 0.7 | 16.8 |
| Babu and Lim | TIP3P | 2.09 | 23.1 | 2.54 | 0.0 | 6.0 | 4.33 | 2.1 | 5.32 | 0.7 | 16.6 |
| Li et al. $\Delta G_{solv}$ | TIP3P | 1.94 | 23.8 | 2.49 | 0.0 | 6.0 | 4.22 | 2.3 | 4.99 | 0.7 | 14.2 |
| Li et al. $R_{Mg^{2+}-O}$ | TIP3P | 2.07 | 23.9 | 2.49 | 0.0 | 6.0 | 4.28 | 2.1 | 5.11 | 0.7 | 14.9 |
| Li et al. CN | TIP3P | 2.03 | 24.5 | 2.49 | 0.0 | 6.0 | 4.25 | 2.2 | 5.25 | 0.7 | 16.1 |
| Li and Merz 12-6-4 | TIP3P | 2.08 | 26.4 | 2.44 | 0.0 | 6.0 | 4.32 | 2.1 | 5.18 | 0.8 | 16.3 |
| Li et al. $\Delta G_{solv}$ | TIP4PEw | 1.89 | 17.5 | 2.60 | 0.0 | 6.0 | 4.09 | 2.5 | 4.83 | 0.6 | 12.9 |
| Li et al. $R_{Mg^{2+}-O}$ | TIP4PEw | 2.09 | 22.3 | 2.54 | 0.0 | 6.0 | 4.31 | 2.2 | 5.03 | 0.7 | 13.8 |
| Li et al. CN | TIP4PEw | 2.04 | 23.1 | 2.53 | 0.0 | 6.0 | 4.27 | 2.3 | 5.01 | 0.7 | 13.8 |
| Li and Merz 12-6-4 | TIP4PEw | 2.08 | 26.2 | 2.49 | 0.0 | 6.0 | 4.26 | 2.2 | 4.98 | 0.8 | 14.3 |
| Experiment | | $2.09 \pm 0.04$ [97] | | | | 6.0 [98] | 4.1–4.2 [98] | | | | 12.0 [98] |

the 12-6 model category along with all the 12-6-4 models. The coordination numbers for the first and second solvation shells, $CN_1$ and $CN_2$, were also calculated. The $CN_1$ value is found to be 6 for all models and agrees with the experimental first coordination number. The calculated $CN_2$ values, on the other hand, are more variable, ranging from about 13–17. These values are consistently larger than the experimental value of 12. The TIP3P $Mg^{2+}$ models tend to have the largest $CN_2$ values compared with both the SPC/E and TIP4PEw $Mg^{2+}$ models.

### Thermodynamics: Solvation free energy values

Experimentally, the standard hydration free energies of ions are typically measured relative to $H^+$. Therefore, the absolute hydration free energy of $H^+$ is required to estimate the absolute hydration free energy of $Mg^{2+}$, which can vary according to different sources. One approach, that of Marcus, uses proton hydration free energies from the National Bureau of Standards compilation and has been heavily used as a reference in $Mg^{2+}$ model development.[14–16,56] Thus, in the present study, the reference standard solvation free energy of $Mg^{2+}$ (−437.4 kcal/mol) follows Marcus's approach where $\Delta G^{\circ}_{solv}$ $H^+ = -1056$ kJ/mol.[99]

Figure 3a summarizes absolute solvation free energies computed for the $Mg^{2+}$ models tested in this study. When computing the solvation free energy using both the SPC/E and the SPC water models for the Åqvist parameter set we see a difference of more than 20 kcal/mol compared to the published value of −455.5 kcal/mol.[54] This is an extreme example of how differences in simulation protocol can affect calculated solvation free energies. Li et al. have recently also tried to reproduce the solvation free energy using the Åqvist parameters and see the same discrepancy.[15] See Supporting Information Table S1 for more information on comparison of computed solvation free energies with published values.

As for the rest of the models, all those that targeted properties other than absolute solvation free energy, including phosphate binding (Mayaan et al.), equilibrium $Mg^{2+}$-O distance or coordination number (Li et al. models), water exchange barrier (Allnér et al.), and relative solvation free energy (Babu and Lim) grossly underestimate the experimental solvation free energy of −437.4 kcal/mol[99] by about 25 (SPC/E Li et al. CN set) to 55 (TIP4PEw Li et al. $R_{Mg^{2+}-O}$ set) kcal/mol. This is a consequence of the static charge force field which uses prepolarized waters with increased permanent dipole moments compared to the gas phase (1.855 D); however, this degree of implicit polarization is optimized for a bulk water environment, rather than in the inner sphere of a divalent ion.

Figure 3b illustrates the behavior of fixed charge $Mg^{2+}$ models in terms of their inability to reproduce both structural and thermodynamic experimental observables and highlights the importance of including polarization effects to this regard. The computed solvation free energies are correlated with the inverse first shell $Mg^{2+}$-O distances; the closer a given parameter gets to the experimental $Mg^{2+}$-O distance, the more under solvated it becomes. TIP4PEw $Mg^{2+}$ models are more under-solvated than SPC/E and TIP3P models at the same $Mg^{2+}$-O
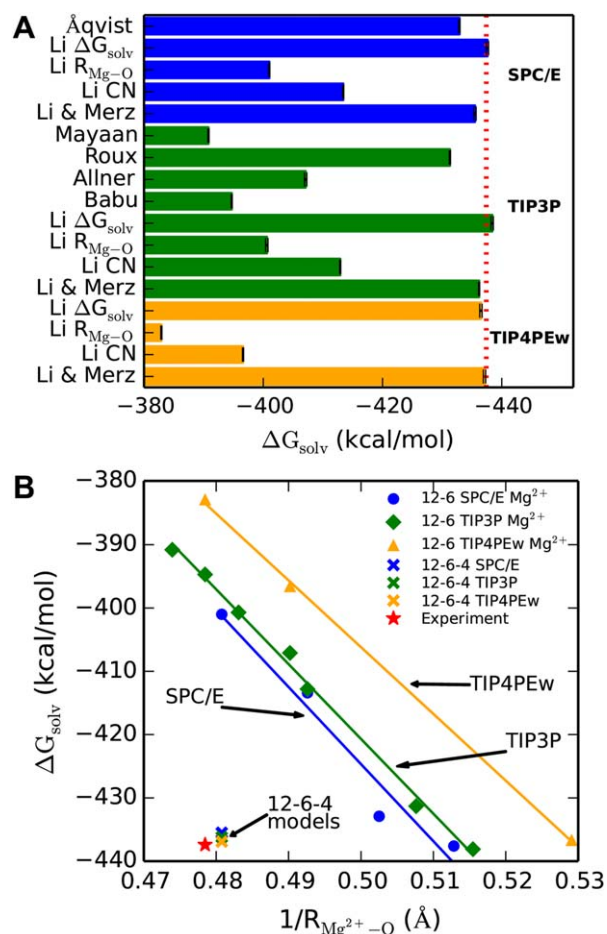


**Figure 3.** a) Summary of solvation free energies collected for the $Mg^{2+}$ models compared with experiment (dashed red line) and b) their correlation with inverse equilibrium $Mg^{2+}$-oxygen distances, both grouped by water model. Depicted error bars are on the order of 0.1 kcal/mol. [Color figure can be viewed in the online issue, which is available at wileyonlinelibrary.com.]

distances. The models which include the induced dipole interaction (i.e., the 12-6-4 models),[16] on the other hand, come very close to reproducing both the experimental hydration free energy and equilibrium $Mg^{2+}$-O distance with our simulation protocol. It should be noted that free energy simulations with nonpolarizable point charge models, in some cases, may reproduce experimental solvation free energies as a result of a cancellation of errors (e.g., lack of electronic polarization counterbalanced by incorrect bare solute charges).[45]

### Kinetics: $Mg^{2+}$-water exchange rates

Water exchange rates for diamagnetic metal ions can in principle be directly obtained from $^{17}O$ NMR relaxation experiments. For $Mg^{2+}$, however, whose first shell waters exchange relatively fast ($>10^4$ $s^{-1}$), a $^{17}O$ NMR bound water resonance is not visible on the NMR spectrum unless addition of either a paramagnetic chemical shift agent or a paramagnetic relaxation agent is employed. There have been two such studies[100,101] which have obtained water exchange rates for $Mg^{2+}$, $5.3 \pm 0.3 \times 10^5$ $s^{-1}$ and $6.7 \pm 0.2 \times 10^5$ $s^{-1}$, the latter of which is used as the reference for this study because the
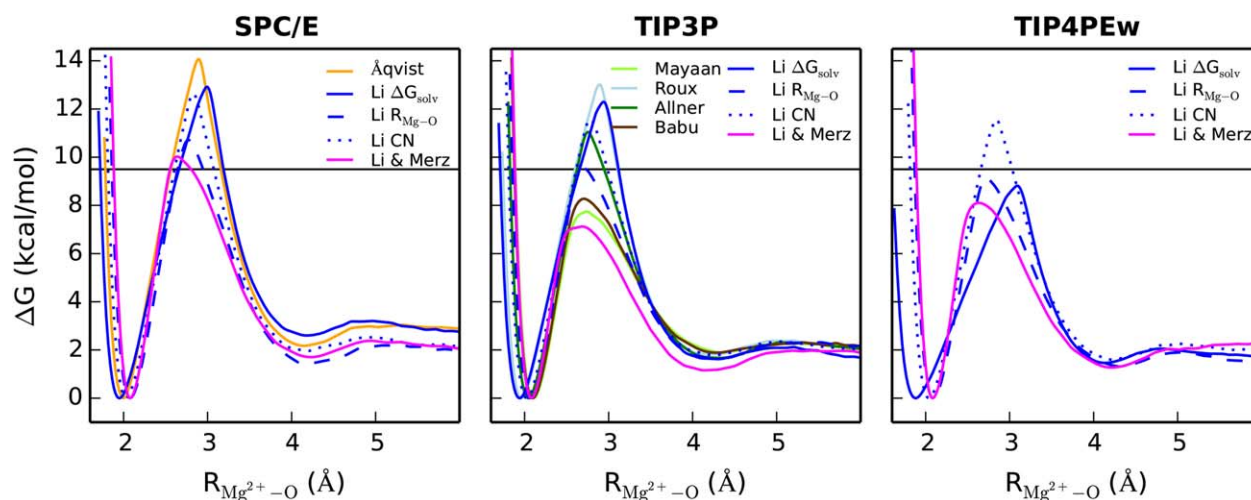
**Figure 4.** Potential of mean force between $Mg^{2+}$ and water oxygen grouped by water model and obtained from the last 2 ns of umbrella sampling data. The horizontal solid line at 9.5 kcal/mol represents the reference $\Delta G^{\dagger}$ that corresponds to the experimental water exchange rate of $6.7 \times 10^5$ s$^{-1}$ with the pre-exponential factor estimated as $k_B T/h$. [Color figure can be viewed in the online issue, which is available at wileyonlinelibrary.com.]

experiment was carried out in 0.18 mol/kg salt concentration versus a 3.52 mol/kg salt concentration in the former study.

To date, there has been relatively little consideration of exchange rates in the development of $Mg^{2+}$ ion models.[98] On the time scales accessible to conventional molecular simulations, the $Mg^{2+}$-water exchange rates are not easily observed directly. Consequently, an alternative method to determine the exchange rate is to compute the free energy profile along an exchange coordinate and use transition state theory to estimate the rate. We have obtained free energy barriers and rates for water exchange in the first solvation shell from potential of mean force profiles (Fig. 4). These free energy profiles show a spread in barrier heights, barrier peak shapes and transition state locations across water model groups (Table 4).

The position of the transition state ($R^{\dagger}$) is correlated with the $R_{Mg^{2+}-O}$ distance for the 12-6 models; the smaller $R_{Mg^{2+}-O}$, the larger $R^{\dagger}$. The 12-6-4 models have $R^{\dagger}$ values around 2.65 Å. About half the models yield barriers that are too high compared with experiment, while the other half yield barriers that are either close to experiment or too low. Interestingly, the models with the highest barrier heights in the SPC/E and TIP3P groups are the Åqvist and Roux models with barriers of 13.9 and 12.9 kcal/mol, respectively. This corresponds to rates that are three and two orders of magnitude lower than the experimental value of $6.7 \times 10^5$ s$^{-1}$.[101] Allnér et al. also computed the barrier to exchange for the Roux model with mTIP3P waters and obtained $12.7 \pm 0.2$ kcal/mol. For the Allnér et al. model itself, however, we calculate a barrier of $10.9 \pm 0.1$ which is 1 kcal/mol higher than the previously published value[98] using a slightly different simulation protocol. Among the Li et al. models there is also a clear trend across water models - the barriers of the $\Delta G_{solv}$, $R_{Mg^{2+}-O}$ and CN sets decrease from SPC/E to TIP3P to TIP4PEw. With the 12-6-4 models, it is interesting to see that although enhanced implicit polarization effects are included in the models and their thermodynamic and structural properties match well with experiment, they do not all have good kinetic behavior. The TIP3P

and TIP4PEw 12-6-4 models overestimate the rate of exchange by an order of magnitude. The SPC/E 12-6-4 model, conversely, is the only one that is within error of the experimental $\log(k_1)$, and performs best with this property compared with the other 16 models in our study even though it was not parametrized to get this property correct. It is also important to note that the Allnér et al. model, which was originally fitted to the experimental exchange rate, is the only other model that we observe to have kinetics on the same order of magnitude as in experiment.

### Mass transport properties: $Mg^{2+}$ diffusion coefficients and viscosities

To our knowledge, the only experimental translational diffusion coefficient at infinite dilution available for $Mg^{2+}$ (as obtained from tracer diffusion experiments of $^{28}Mg$ in $MgCl_2$ solutions) is $0.706 \times 10^{-5}$ cm$^2$/s[102] and this value will be used as a reference to compare with computed diffusion coefficients. The experimental viscosity of water,[103] $8.903 \times 10^{-4}$ kgm$^{-1}$s$^{-1}$, will also be compared with our calculated solvent viscosities.

Despite its importance as a fundamental bulk transport property, diffusion coefficients are often neglected in the parametrization of $Mg^{2+}$ ion models. Accurate calculation of the diffusion coefficient at infinite dilution requires consideration of the size of the simulation cell, as well as consideration of systematic errors in the diffusion of modeled water molecules. Figure 5 illustrates the dependence of the calculated diffusion coefficients on the box size for four $Mg^{2+}$-water systems consisting of 1 $Mg^{2+}$ ion and either 540, 1028, 2310, or 4394 water molecules.

In order to directly compare $Mg^{2+}$ diffusion coefficients ($D_o^{sim}$) with experiment in the dilute limit using different water models, they must be rescaled ($D_o$) to correct for systematic errors in the diffusion coefficients of the water models themselves (see discussion in Methods section). Table 5 lists the

**Table 4.** Summary of data extracted from free energy profiles for inner-sphere water exchange: $R^\dagger$: transition state distance (Å), **A**: pre-exponential factor (fs$^{-1}$), $\Delta G^\dagger$: activation free energy (kcal/mol), $k_1{}^\dagger$: first solvation shell water exchange rate (s$^{-1}$). Standard deviations come from four consecutive 2 ns segments of data.

| Model | Water model | $R^\dagger$ | A | $\Delta G^\dagger$ | $\log(k_1)$ | $k_1$ |
|---|---|---|---|---|---|---|
| Åqvist | SPC/E | 2.88 ± 0.01 | 0.015 | 13.9 ± 0.1 | 3.0 ± 0.1 | $9.5 \times 10^2$ |
| Li et al. $\Delta G_{solv}$ | SPC/E | 2.98 ± 0.01 | 0.013 | 12.7 ± 0.3 | 3.8 ± 0.4 | $6.4 \times 10^3$ |
| Li et al. $R_{Mg^{2+}-O}$ | SPC/E | 2.76 ± 0.01 | 0.014 | 10.9 ± 0.3 | 5.2 ± 0.4 | $1.5 \times 10^5$ |
| Li et al. CN | SPC/E | 2.84 ± 0.01 | 0.014 | 12.4 ± 0.1 | 4.1 ± 0.1 | $1.1 \times 10^4$ |
| Li and Merz 12-6-4 | SPC/E | 2.66 ± 0.02 | 0.017 | 10.2 ± 0.3 | 5.7 ± 0.4 | $5.5 \times 10^5$ |
| Mayaan et al. | TIP3P | 2.72 ± 0.01 | 0.015 | 7.8 ± 0.1 | 7.5 ± 0.1 | $2.9 \times 10^7$ |
| Roux | TIP3P | 2.89 ± 0.00 | 0.014 | 12.9 ± 0.1 | 3.7 ± 0.1 | $4.8 \times 10^3$ |
| Allnér et al. | TIP3P | 2.75 ± 0.01 | 0.015 | 10.9 ± 0.1 | 5.2 ± 0.1 | $1.5 \times 10^5$ |
| Babu and Lim | TIP3P | 2.69 ± 0.02 | 0.015 | 8.2 ± 0.1 | 7.2 ± 0.1 | $1.5 \times 10^7$ |
| Li et al. $\Delta G_{solv}$ | TIP3P | 2.95 ± 0.01 | 0.012 | 12.6 ± 0.2 | 3.9 ± 0.3 | $7.2 \times 10^3$ |
| Li et al. $R_{Mg^{2+}-O}$ | TIP3P | 2.70 ± 0.00 | 0.015 | 9.6 ± 0.1 | 6.1 ± 0.1 | $1.3 \times 10^6$ |
| Li et al. CN | TIP3P | 2.78 ± 0.00 | 0.015 | 11.6 ± 0.1 | 4.7 ± 0.1 | $4.5 \times 10^4$ |
| Li and Merz 12-6-4 | TIP3P | 2.68 ± 0.00 | 0.017 | 7.5 ± 0.2 | 7.7 ± 0.3 | $5.2 \times 10^7$ |
| Li et al. $\Delta G_{solv}$ | TIP4PEw | 3.10 ± 0.01 | 0.010 | 8.7 ± 0.1 | 6.6 ± 0.1 | $4.2 \times 10^6$ |
| Li et al. $R_{Mg^{2+}-O}$ | TIP4PEw | 2.73 ± 0.01 | 0.015 | 9.4 ± 0.2 | 6.3 ± 0.3 | $1.9 \times 10^6$ |
| Li et al. CN | TIP4PEw | 2.84 ± 0.01 | 0.014 | 11.5 ± 0.1 | 4.7 ± 0.1 | $5.1 \times 10^4$ |
| Li and Merz 12-6-4 | TIP4PEw | 2.63 ± 0.00 | 0.016 | 8.4 ± 0.2 | 7.1 ± 0.3 | $1.1 \times 10^7$ |
| Experiment[101] | | | | | 5.8 | $6.7 \pm 0.2 \times 10^5$ |

scaled values of the simulated diffusion coefficients, viscosities and hydrodynamic radii at infinite dilution that will be referred to for the remainder of this discussion (Supporting Information Table S5 lists the corresponding unscaled values for reference).

Overall, the calculated values for the scaled infinite dilution diffusion coefficients ranged between 0.723 and 0.813 $\times$ $10^{-5}$ cm$^2$/s, slightly higher than the experimental value of 0.706 $\times$ $10^{-5}$ cm$^2$/s. No obvious trend is evident from the diffusion results (Table 5), although it should be pointed out that the standard deviations for individual diffusion coefficient values are fairly large relative to the differences between average values making any conclusion about average trends likely not statistically significant. Individual diffusion coefficients for the SPC/E Mg$^{2+}$ models are most similar while the TIP4PEw Mg$^{2+}$ models show the most variation for a given box size. Although none of the Mg$^{2+}$ SPC/E models were originally parametrized

to match translation diffusion, their computed scaled $D_o$ values are all within error of the experimental translational diffusion coefficient. The same can be said for two of the TIP4PEw Mg$^{2+}$ models, the Li et al. $\Delta G_{solv}$ and CN sets. All the TIP3P Mg$^{2+}$ models, on the other hand, have scaled diffusion coefficients that are slightly too high (e.g., beyond the simulated standard deviations).

Solvent viscosities can be extracted from the slopes of the (scaled) $D_{PBC}$ versus $1/L$ plot as previously discussed and these are summarized in Table 5. The Roux model, which has the largest scaled diffusion coefficient, has the smallest scaled solvent viscosity among all the models, 7.64 $\times$ $10^{-4}$ kgm$^{-1}$s$^{-1}$. The SPC/E Li et al. CN model is on the other end of the spectrum with the smallest scaled diffusion coefficient and largest scaled solvent viscosity of 9.81 $\times$ $10^{-4}$ kgm$^{-1}$s$^{-1}$. It is also interesting to note that although the SPC/E Li et al. CN model
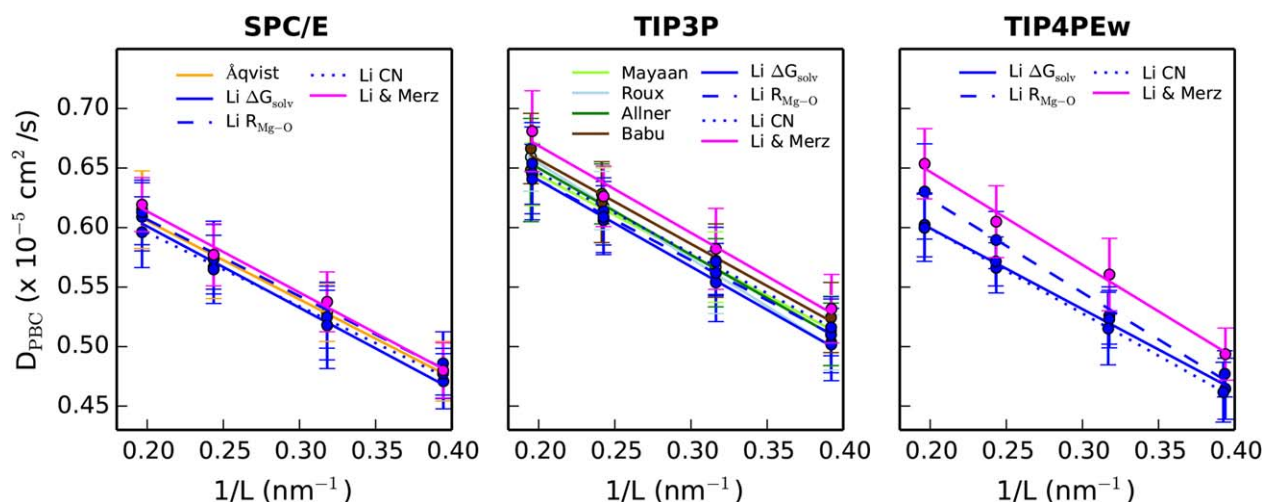


**Figure 5.** Dependence of calculated diffusion coefficients for Mg$^{2+}$ models ($D_{PBC}$) scaled by the ratio of experimental and computed water diffusion coefficients ($\frac{D_o^w}{D_o^{sw}}$) to correct for diffusion errors in the water models. [Color figure can be viewed in the online issue, which is available at wileyonlinelibrary.com.]

**Table 5.** Scaled infinite dilution diffusion coefficients ($\times 10^{-5}$ cm²/s) and hydrodynamic radii (Å) for the $Mg^{2+}$ parameters and the respective solvent viscosities ($\times 10^{-4}$ kgm$^{-1}$s$^{-1}$). $D_o$, $\eta$ and $r$ are $D_o^{sim}$, $\eta^{sim}$, and $r^{sim}$ (Supporting Information Table S5) rescaled by $\frac{D_o^w}{D_o^{sim}}$ (see discussion in Methods) to correct for errors in the diffusion coefficients of the water models.

| Model | Water model | $D_o$ | $\eta$ | $r$ |
|---|---|---|---|---|
| Åqvist | SPC/E | 0.741 ± 0.057 | 9.23 ± 0.36 | 3.19 |
| Li et al. $\Delta G_{solv}$ | SPC/E | 0.736 ± 0.052 | 9.16 ± 0.28 | 3.24 |
| Li et al. $R_{Mg^{2+}-O}$ | SPC/E | 0.735 ± 0.052 | 9.67 ± 0.23 | 3.07 |
| Li et al. CN | SPC/E | 0.723 ± 0.052 | 9.81 ± 0.21 | 3.08 |
| Li and Merz 12-6-4 | SPC/E | 0.748 ± 0.044 | 9.19 ± 0.24 | 3.18 |
| Mayaan et al. | TIP3P | 0.779 ± 0.052 | 9.18 ± 0.11 | 3.05 |
| Roux | TIP3P | 0.817 ± 0.049 | 7.64 ± 0.11 | 3.50 |
| Allnér et al. | TIP3P | 0.802 ± 0.068 | 8.24 ± 0.27 | 3.30 |
| Babu and Lim | TIP3P | 0.798 ± 0.057 | 8.79 ± 0.28 | 3.11 |
| Li et al. $\Delta G_{solv}$ | TIP3P | 0.790 ± 0.065 | 8.32 ± 0.10 | 3.32 |
| Li et al. $R_{Mg^{2+}-O}$ | TIP3P | 0.771 ± 0.057 | 9.38 ± 0.10 | 3.02 |
| Li et al. CN | TIP3P | 0.783 ± 0.059 | 9.09 ± 0.29 | 3.07 |
| Li and Merz 12-6-4 | TIP3P | 0.813 ± 0.059 | 8.59 ± 0.41 | 3.13 |
| Li et al. $\Delta G_{solv}$ | TIP4PEw | 0.744 ± 0.051 | 8.70 ± 0.21 | 3.37 |
| Li et al. $R_{Mg^{2+}-O}$ | TIP4PEw | 0.779 ± 0.061 | 7.97 ± 0.18 | 3.52 |
| Li et al. CN | TIP4PEw | 0.740 ± 0.050 | 8.77 ± 0.10 | 3.36 |
| Li and Merz 12-6-4 | TIP4PEw | 0.801 ± 0.052 | 8.01 ± 0.22 | 3.40 |
| Experiment | | 0.706[102] | 8.903[103] | |

has the scaled diffusion coefficient that matches experiment best, the corresponding scaled solvent viscosity is too high compared to the experimental value.

By applying the Stokes–Einstein relation[65] we can also estimate the effective hydrodynamic radius of the $Mg^{2+}$ ion models using our computed (scaled) $D_o$ values and solvent viscosities:

$$D = \frac{k_B T}{6\pi\eta r} \tag{10}$$

where $k_B$ is the Boltzmann constant, $T$ is the temperature in K, $\eta$ is the solvent viscosity and $r$ is the radius of a spherical particle. Comparing the simulated values from Table 5 gives effective hydrodynamic radii in the ranges of 3.07–3.24, 3.02–3.50, and 3.36–3.50 Å for SPC/E, TIP3P and TIP4PEw, respectively.

## Conclusion

The importance of $Mg^{2+}$ ions for biomolecular structure, dynamics and function has been a driving force for the development of $Mg^{2+}$ models in recent years.

In an effort to better understand the strengths and weaknesses of an existing set of 17 different $Mg^{2+}$ ion models, we evaluated their ability to simultaneously reproduce structural, thermodynamic, kinetic and mass transport properties in aqueous solution. These represent a balanced set of solution properties that serve as a useful departure point from which robust models for molecular dynamics simulations of biological processes can be developed by tuning pairwise interaction parameters.

Certain bulk properties such as the first shell $Mg^{2+}$-O distances and solvation free energies were observed to be correlated

to the minimum energy distances and adiabatic binding energies from gas phase binding energy scans. Most of the models considered either overestimate or underestimate the inner shell water exchange barrier by several kcal/mol. On the other hand, mass transport properties were observed to be somewhat insensitive to the models. The simple 12-6 models were shown to have considerable limitations regardless of the water model used or the specific LJ parameters. These models were not able to simultaneously reproduce both structural and thermodynamic properties with reasonable accuracy. The 12-6-4 models, on the other hand, offer respectable improvement, particularly with respect to matching both the radial distribution function and solvation free energy. One model in particular, the SPC/E 12-6-4 model of Li et al., performs extremely well across all properties (within statistical confidence) despite only being originally parametrized to match structure and thermodynamics.

This detailed analysis of the solution properties predicted by several $Mg^{2+}$ models used in molecular simulations provides a baseline from which to gauge progress and direct future effort. In progressing toward improved force field models for simulations of biomolecules, and in particular RNA, under different ionic conditions, it is important to properly balance the ion–water, ion–ion, and ion–biomolecule interactions. This underscores the importance of testing the models with respect to binding to protein, DNA and RNA systems, and comparing simulation results against quantitative measurements such as specific binding constants and exchange rates, and results from ion counting experiments (including ion competition).

[1] D. E. Draper, *RNA* **2004**, *10*, 335.
[2] E. Freisinger, R. K. O. Sigel, *Coordin. Chem. Rev.* **2007**, *251*, 1834.
[3] R. K. O. Sigel, H. Sigel, *Acc. Chem. Res.* **2010**, *43*, 974.
[4] C. Hammann, D. G. Norman, D. M. J. Lilley, *Proc. Natl. Acad. Sci. USA* **2001**, *98*, 5503.
[5] R. Das, K. J. Travers, Y. Bai, D. Herschlag, *J. Am. Chem. Soc.* **2005**, *127*, 8272.
[6] A. Laederach, I. Shcherbakova, M. A. Jonikas, R. B. Altman, M. Brenowitz, *Proc. Natl. Acad. Sci. USA* **2007**, *104*, 7045.
[7] J. K. Frederiksen, N.-S. Li, R. Das, D. Herschlag, J. A. Piccirilli, *RNA* **2012**, *18*, 1123.
[8] A. M. Pyle, *J. Biol. Inorg. Chem.* **2002**, *7*, 679.
[9] V. J. DeRose, *Curr. Opin. Struct. Biol.* **2003**, *13*, 317.
[10] J. Schnabl, R. K. O. Sigel, *Curr. Opin. Chem. Biol.* **2010**, *14*, 269.

[11] A. R. Ferré-D'Amaré, W. G. Scott, *Cold Spring Harb. Perspect. Biol.* **2010**, *2*, a003574.

[12] W. L. Ward, K. Plakos, V. J. DeRose, *Chem. Rev.* **2014**, *114*, 4318.

[13] J. M. Martínez, R. R. Pappalardo, E. S. Marcos, *J. Am. Chem. Soc.* **1999**, *121*, 3175.

[14] C. S. Babu, C. Lim, *J. Phys. Chem. A* **2006**, *110*, 691.

[15] P. Li, B. P. Roberts, D. K. Chakravorty, K. M. Merz, Jr., *J. Chem. Theory Comput.* **2013**, *9*, 2733.

[16] P. Li, K. M. Merz, Jr., *J. Chem. Theory Comput.* **2014**, *10*, 289.

[17] D. Case, V. Babin, J. Berryman, R. Betz, Q. Cai, D. Cerutti, T. Cheatham III, T. Darden, R. Duke, H. Gohlke, A. W. Goetz, S. Gusarov, N. Homeyer, P. Janowski, J. Kaus, I. Kolossvàry, A. Kovalenko, T. S. Lee, S. LeGrand, T. Luchko, R. Luo, B. Madej, K. M. Merz, F. Paesani, D. R. Roe, A. Roitberg, C. Sagui, R. Salomon-Ferrer, G. Seabra, C. L. Simmerling, W. Smith, J. Swails, R. C. Walker, J. Wang, R. M. Wolf, X. Wu, P. A. Kollman, *AMBER 14*, University of California, San Francisco, San Francisco, CA, **2014**.

[18] W. D. Cornell, P. Cieplak, C. I. Bayly, I. R. Gould, K. M. Merz, Jr., D. M. Ferguson, D. C. Spellmeyer, T. Fox, J. W. Caldwell, P. A. Kollman, *J. Am. Chem. Soc.* **1995**, *117*, 5179.

[19] J. Wang, P. Cieplak, P. A. Kollman, *J. Comput. Chem.* **2000**, *21*, 1049.

[20] A. Pérez, I. Marchán, D. Svozil, J. Sponer, T. E. Cheatham III, C. A. Laughton, M. Orozco, *Biophys. J.* **2007**, *92*, 3817.

[21] M. Zgarbová, M. Otyepka, J. Šponer, A. Mládek, P. Banáš, T. E. Cheatham III, P. Jurečka, *J. Chem. Theory Comput.* **2011**, *7*, 2886.

[22] A. D. MacKerell, Jr., N. K. Banavali, *J. Comput. Chem.* **2000**, *21*, 105.

[23] N. Foloppe, A. D. MacKerell, Jr., *J. Comput. Chem.* **2000**, *21*, 86.

[24] C. Oostenbrink, A. Villa, A. E. Mark, W. F. van Gunsteren, *J. Comput. Chem.* **2004**, *25*, 1656.

[25] W. L. Jorgensen, D. S. Maxwell, J. Tirado-Rives, *J. Am. Chem. Soc.* **1996**, *118*, 11225.

[26] G. A. Kaminski, R. A. Friesner, J. Tirado-Rives, W. L. Jorgensen, *J. Phys. Chem. B* **2001**, *105*, 6474.

[27] J. W. Ponder, C. Wu, P. Ren, V. S. Pande, J. D. Chodera, M. J. Schnieders, I. Haque, D. L. Mobley, D. S. Lambrecht, R. A. DiStasio, Jr., M. Head-Gordon, G. N. I. Clark, M. E. Johnson, T. Head-Gordon, *J. Phys. Chem. B* **2010**, *114*, 2549.

[28] D. Jiao, C. King, A. Grossfield, T. A. Darden, P. Ren, *J. Phys. Chem. B* **2006**, *110*, 18553.

[29] A. Grossfield, P. Ren, J. W. Ponder, *J. Am. Chem. Soc.* **2003**, *125*, 15671.

[30] G. Lamoureux B. Roux, *J. Phys. Chem. B* **2006**, *110*, 3308.

[31] J.-P. Piquemal, L. Perera, G. A. Cisneros, P. Ren, L. G. Pedersen, T. A. Darden, *J. Chem. Phys.* **2006**, *125*, 054511.

[32] H. Yu, T. W. Whitfield, E. Harder, G. Lamoureux, I. Vorobyov, V. M. Anisimov, A. D. MacKerell, Jr., B. Roux, *J. Chem. Theory Comput.* **2010**, *6*, 774.

[33] D. Spångberg, K. Hermansson, *J. Chem. Phys.* **2004**, *120*, 4829.

[34] M. B. Peters, Y. Yang, B. Wang, L. Füsti-Molnár, M. N. Weaver, K. M. Merz, Jr., *J. Chem. Theory Comput.* **2010**, *6*, 2935.

[35] J. Bredenberg, L. Nilsson, *Int. J. Quantum Chem.* **2001**, *83*, 230.

[36] S. C. Hoops, K. W. Anderson, K. M. Merz, Jr., *J. Am. Chem. Soc.* **1991**, *113*, 8262.

[37] R. H. Stote, M. Karplus, *Proteins* **1995**, *23*, 12.

[38] L. Helm, A. E. Merbach, *Coord. Chem. Rev.* **1999**, *187*, 151.

[39] A. Saxena, D. Sept, *J. Chem. Theory Comput.* **2013**, *9*, 3538.

[40] J. Åqvist, A. Warshel, *J. Am. Chem. Soc.* **1990**, *112*, 2860.

[41] Y.-P. Pang, *J. Mol. Model.* **1999**, *5*, 196.

[42] Y.-P. Pang, K. Xu, J. El Yazal, F. G. Prendergast, *Protein Sci.* **2000**, *9*, 1857.

[43] P. Oelschlaeger, M. Klahn, W. A. Beard, S. H. Wilson, A. Warshel, *J. Mol. Biol.* **2007**, *366*, 687.

[44] J. E. Jones, *Proc. R. Soc. Lond. A* **1924**, *106*, 463.

[45] I. V. Leontyev, A. A. Stuchebrukhov, *Phys. Chem. Chem. Phys.* **2011**, *13*, 2613.

[46] I. V. Leontyev, A. A. Stuchebrukhov, *J. Chem. Theory Comput.* **2010**, *6*, 1498.

[47] I. V. Leontyev, A. A. Stuchebrukhov, *J. Chem. Phys.* **2014**, *141*, 014103.

[48] M. Kohagen, P. E. Mason, P. Jungwirth, *J. Phys. Chem. B* **2014**, *118*, 7902.

[49] E. Pluhařová, P. E. Mason, P. Jungwirth, *J. Phys. Chem. A* **2013**, *117*, 11766.

[50] P. E. Mason, E. Wernersson, P. Jungwirth, *J. Phys. Chem. B* **2012**, *116*, 8145.

[51] H. J. C. Berendsen, J. R. Grigera, T. P. Straatsma, *J. Phys. Chem.* **1987**, *91*, 6269.

[52] W. L. Jorgensen, J. Chandrasekhar, J. D. Madura, R. W. Impey, M. L. Klein, *J. Chem. Phys.* **1983**, *79*, 926.

[53] H. W. Horn, W. C. Swope, J. W. Pitera, J. D. Madura, T. J. Dick, G. L. Hura, T. Head-Gordon, *J. Chem. Phys.* **2004**, *120*, 9665.

[54] J. Åqvist, *J. Phys. Chem.* **1990**, *94*, 8021.

[55] E. Mayaan, A. Moser, A. D. MacKerell, Jr., D. M. York, *J. Comput. Chem.* **2007**, *28*, 495.

[56] O. Allnér, L. Nilsson, A. Villa, *J. Chem. Theory Comput.* **2012**, *8*, 1493.

[57] E. Neria, S. Fischer, M. Karplus, *J. Chem. Phys.* **1996**, *105*, 1902.

[58] B. R. Brooks, C. L. Brooks, III, A. D. MacKerell, Jr., L. Nilsson, R. J. Petrella, B. Roux, Y. Won, G. Archontis, C. Bartels, S. Boresch, A. Caflisch, L. Caves, Q. Cui, A. R. Dinner, M. Feig, S. Fischer, J. Gao, M. Hodoscek, W. Im, K. Kuczera, T. Lazaridis, J. Ma, V. Ovchinnikov, E. Paci, R. W. Pastor, C. B. Post, J. Z. Pu, M. Schaefer, B. Tidor, R. M. Venable, H. L. Woodcock, X. Wu, W. Yang, D. M. York, M. Karplus, *J. Comput. Chem.* **2009**, *30*, 1545.

[59] D. Frenkel, B. Smit, Understanding Molecular Simulation, Academic Press: San Diego, CA, **2002**.

[60] J. G. Kirkwood, *J. Chem. Phys.* **1935**, *3*, 300.

[61] T. Steinbrecher, I. Joung, D. A. Case, *J. Comput. Chem.* **2011**, *32*, 3253.

[62] T.-S. Lee, B. K. Radak, A. Pabis, D. M. York, *J. Chem. Theory Comput.* **2013**, *9*, 153.

[63] T.-S. Lee, B. K. Radak, M. Huang, K.-Y. Wong, D. M. York, *J. Chem. Theory Comput.* **2014**, *10*, 24.

[64] M. R. Shirts, J. D. Chodera, *J. Chem. Phys.* **2008**, *129*, 124105.

[65] A. Grossfield, WHAM: the weighted histogram analysis method, version 2.0.4; Available at: http://membrane.urmc.rochester.edu/content/wham (accessed April **2012**).

[66] A. Einstein, *Annalen der Physik* **1905**, *17*, 549.

[67] B. Dünweg, K. Kremer, *J. Chem. Phys.* **1993**, *99*, 6983.

[68] S. Obst, H. Bradaczek, *J. Phys. Chem.* **1996**, *100*, 15677.

[69] D. Spångberg, K. Hermansson, *J. Chem. Phys.* **2003**, *119*, 7263.

[70] I.-C. Yeh, G. Hummer, *J. Phys. Chem. B* **2004**, *108*, 15873.

[71] S. Tazi, A. Boţan, M. Salanne, V. Marry, P. Turq, B. Rotenberg, *J. Phys. Condens. Matter* **2012**, *24*, 284117.

[72] T. Darden, D. York, L. Pedersen, *J. Chem. Phys.* **1993**, *98*, 10089.

[73] J. P. Ryckaert, G. Ciccotti, H. J. C. Berendsen, *J. Comput. Phys.* **1977**, *23*, 327.

[74] H. J. C. Berendsen, J. P. M. Postma, W. F. van Gunsteren, A. Dinola, J. R. Haak, *J. Chem. Phys.* **1984**, *81*, 3684.

[75] P. Turq, F. Lantelme, H. L. Friedman, *J. Chem. Phys.* **1977**, *66*, 3039.

[76] M. J. Frisch, G. W. Trucks, H. B. Schlegel, G. E. Scuseria, M. A. Robb, J. R. Cheeseman, G. Scalmani, V. Barone, B. Mennucci, G. A. Petersson, H. Nakatsuji, M. Caricato, X. Li, H. P. Hratchian, A. F. Izmaylov, J. Bloino, G. Zheng, J. L. Sonnenberg, M. Hada, M. Ehara, K. Toyota, R. Fukuda, J. Hasegawa, M. Ishida, T. Nakajima, Y. Honda, O. Kitao, H. Nakai, T. Vreven, J. A. Montgomery, Jr., A., J. E. Peralta, F. Ogliaro, M. Bearpark, J. J. Heyd, E. Brothers, K. N. Kudin, V. N. Staroverov, R. Kobayashi, J. Normand, K. Raghavachari, A. Rendell, J. C. Burant, S. S. Iyengar, J. Tomasi, M. Cossi, N. Rega, J. M. Millam, M. Klene, J. E. Knox, J. B. Cross, V. Bakken, C. Adamo, J. Jaramillo, R. Gomperts, R. E. Stratmann, O. Yazyev, A. J. Austin, R. Cammi, C. Pomelli, J. W. Ochterski, R. L. Martin, K. Morokuma, V. G. Zakrzewski, G. A. Voth, P. Salvador, J. J. Dannenberg, S. Dapprich, A. D. Daniels, O. Farkas, J. B. Foresman, J. V. Ortiz, J. Cioslowski, D. J. Fox, Gaussian09 Revision D.01, Gaussian: Wallingford CT **2009**.

[77] W. Humphrey, A. Dalke, K. Schulten, *J. Mol. Graphics* **1996**, *14*, 33.

[78] J. W. Kaus, L. T. Pierce, R. C. Walker, J. A. McCammon, *J. Chem. Theory Comput.* **2013**, *9*, 4131.

[79] S. C. Harvey, R. K. Z. Tan, T. E. Cheatham III, *J. Comp. Chem.* **1998**, *19*, 726.

[80] D. Cottrell, P. F. Tupper, *BIT Num. Math.* **2007**, *47*, 507.

[81] G. Lamoureux, B. Roux, *J. Chem. Phys.* **2003**, *119*, 3025.

[82] J. E. Basconi, M. R. Shirts, *J. Chem. Theory Comput.* **2013**, *9*, 2887.

[83] H. C. Andersen, *J. Chem. Phys.* **1980**, *72*, 2384.

[84] S. Nosé, *J. Chem. Phys.* **1984**, *81*, 511.

[85] W. G. Hoover, *Phys. Rev. A* **1985**, *31*, 1695.

[86] G. J. Martyna, M. L. Klein, M. Tuckerman, *J. Chem. Phys.* **1992**, *97*, 2635.

[87] M. R. Shirts, *J. Chem. Theory Comput.* **2013**, *9*, 909.

[88] E. Guàrdia, G. Sesé, J. A. Padró, S. G. Kalko, *J. Solut. Chem.* **1999**, *28*, 1113.

[89] A. K. Dorosh, A. F. Skryshevskii, *J. Struct. Chem.* **1964**, *5*, 842.

[90] R. Caminiti, G. Licheri, G. Piccaluga, G. Pinna, *J. Appl. Cryst.* **1979**, *12*, 34.

[91] W. Bol, G. J. A. Gerrits, C. L. van Panthaleon van Eck, *J. Appl. Cryst.* **1970**, *3*, 486.

[92] J. N. Albright, *J. Chem. Phys.* **1972**, *56*, 3783.

[93] R. Caminiti, *Chem. Phys. Lett.* **1982**, *88*, 103.

[94] N. A. Matwiyoff, H. Taube, *J. Am. Chem. Soc.* **1968**, *90*, 2796.

[95] B. J. Vogrin, P. S. Knapp, W. L. Flint, A. Anton, G. Highberger, E. R. Malinowski, *J. Chem. Phys.* **1971**, *54*, 178.

[96] M. L. Lesiecki, J. W. Nibler, *J. Chem. Phys.* **1976**, *64*, 871.

[97] Y. Marcus, *Chem. Rev.* **1988**, *88*, 1475.

[98] H. Ohtaki, T. Radnai, *Chem. Rev.* **1993**, *93*, 1157.

[99] Y. Marcus, *J. Chem. Soc. Faraday Trans.* **1991**, *87*, 2995.

[100] J. Neely, R. Connick, *J. Am. Chem. Soc.* **1970**, *92*, 3476.

[101] A. Bleuzen, P.-A. Pittet, L. Helm, A. E. Merbach, *Magn. Reson. Chem.* **1997**, *35*, 765.

[102] R. P. W. J. Struis, J. de Bleijser, J. C. Leyte, *J. Phys. Chem.* **1987**, *91*, 6309.

[103] L. Korson, W. Drost-Hansen, F. J. Millero, *J. Phys. Chem.* **1969**, *73*, 34.